

This is a repository copy of *Improved startup control of aero doubly salient electromagnetic starter generator based on optimised currents distribution with advanced angle commutation*.

White Rose Research Online URL for this paper:

<https://eprints.whiterose.ac.uk/203438/>

Version: Published Version

Article:

Zhou, Xingwei, Liu, Peixin, Niu, Shuangxia et al. (2 more authors) (2023) Improved startup control of aero doubly salient electromagnetic starter generator based on optimised currents distribution with advanced angle commutation. IET Electric Power Applications. ISSN 1751-8679

<https://doi.org/10.1049/elp2.12338>

Reuse



This article is distributed under the terms of the Creative Commons Attribution-NonCommercial-NoDerivs (CC BY-NC-ND) licence. This licence only allows you to download this work and share it with others as long as you credit the authors, but you can't change the article in any way or use it commercially. More information and the full terms of the licence here: <https://creativecommons.org/licenses/>

Takedown

If you consider content in White Rose Research Online to be in breach of UK law, please notify us by emailing eprints@whiterose.ac.uk including the URL of the record and the reason for the withdrawal request.

ORIGINAL RESEARCH

Improved startup control of aero doubly salient electromagnetic starter generator based on optimised currents distribution with advanced angle commutation

Xingwei Zhou¹  | Peixin Liu¹  | Shuangxia Niu² | Xing Zhao³ | Li Zhang¹

¹College of Energy and Electrical Engineering, Hohai University, Nanjing, China

²Department of Electrical Engineering, The Hong Kong Polytechnic University, Kowloon, Hong Kong

³Department of Electrical Engineering, University of York, York, UK

Correspondence

Xingwei Zhou.

Email: zhxw@hhu.edu.cn

Funding information

National Natural Science Foundation of China, Grant/Award Number: 51907051; Hong Kong Scholar Program, Grant/Award Number: XJ2021015; Jiangsu Province Graduate Student Practice Innovation Program, Grant/Award Number: SJCX22_0181; The open fund Project of Jiangsu Key Laboratory of Power Transmission & Distribution Equipment Technology, Grant/Award Number: 2021JSSPd09

Abstract

Doubly salient electromagnetic machine (DSEM) can constitute a competitive rugged starter generator (SG) system. But under the traditional startup control method, the field current is set to the rated value regardless of speed or load torque conditions, and the phase currents are controlled with standard angle commutation, bringing in large power loss as well as non-negligible torque ripple. To overcome these shortcomings, based on the established DSEM power loss calculation model, a currents distribution strategy is proposed according to the obtained quantitative relationship between DSEM power loss and field current under multiple speed and load torque conditions. Then, to identify the load torque for practical implementation, a novel torque observer is designed based on back propagation (BP) neural network algorithm. Afterwards, to further improve the startup torque performance, currents distribution with advanced angle commutation (AAC) strategy is put forward, where the optimal advanced angle is selected from a 3-D lookup table to achieve the minimal commutation torque ripple. Under the proposed control strategies, DSEM power loss as well as the output torque ripple are desired to be decreased, the simulation and experimental results on a 12/8-pole DSEM prototype verify the correctness and feasibility of the proposed strategies under multiple operating conditions.

KEYWORDS

AC motor drives, reluctance motor drives

1 | INTRODUCTION

With the increasing improvement of aircraft performance and the increasing number of airborne electrical equipment, multi-electric aircraft technology has become an important direction of aircraft development, which puts forward higher requirements for the aviation power system [1–3]. Starting Generator (SG) technology enables the dual function of starting and generating power with just one motor, which eliminates the traditional starter, simplifies engine accessories, and improves reliability and power density. It has become the core technology of modern aviation electrical system [4, 5]. DSEM owns the advantages of solid structure, high reliability, strong fault tolerance and strong excitation regulation ability, it can constitute a competitive SG [6–8].

Efficiency is an important index for aero SG, to improve the operating efficiency of DSEM SG, the main optimisation is to reduce the loss, especially to minimise the iron loss and copper loss. The current research is mainly realized through motor structure optimisation and control strategy improvement. In the former category, [9] applied the four layer winding structure to the motor, which can significantly reduce the iron loss while suppressing harmonics. To further improve torque density, integrated stator windings are used to replace the armature and field windings in traditional hybrid excitation motors [10]. In addition, a novel doubly salient motor with non-overlapping field windings was designed, and the electromagnetic performance of motors with different combinations of stator and rotor poles were studied, balancing high torque density and wide magnetic flux regulation range [11].

This is an open access article under the terms of the [Creative Commons Attribution-NonCommercial-NoDerivs](https://creativecommons.org/licenses/by-nc-nd/4.0/) License, which permits use and distribution in any medium, provided the original work is properly cited, the use is non-commercial and no modifications or adaptations are made.

© 2023 The Authors. *IET Electric Power Applications* published by John Wiley & Sons Ltd on behalf of The Institution of Engineering and Technology.

In the field of control strategy improvement, current ripple suppression method is studied [12], which is helpful to improve torque performance. In ref. [13], a dual-pulse mode control of high-speed DSEM is adopted to reduce motor loss in a wide speed range. In order to improve the static performance and robustness of the motor, the indirect adaptive fuzzy control is applied to the generator voltage regulation system [14]. The above methods only control the armature current and do not give full play to the flexible field regulation ability of DSEM. To solve this problem, particle swarm algorithm was introduced to study the current distribution strategy, and the efficiency of the system was improved with the goal of minimising copper loss [15]. In addition, a new DSEM control strategy was proposed, in which the armature current was set to the rated value and the output torque was adjusted by adjusting the field current [16]. However, due to the large inductance of the field winding, the dynamic performance is degraded. In order to improve the dynamic performance, [17] proposed a new conduction angle control strategy in power generation applications to minimise the field current increment in the dynamic process.

Nevertheless, currents distribution cannot perfectly solve the problem of large torque ripple during standard angle commutation (SAC), and angle control is one of the effective ways to optimise motor commutation torque ripple [18], generally including three-state control, six-state control, nine-state control etc. [19–21]. In recent years, some new optimisation methods have been proposed. For example, a self-tuning control method of the multi-angle alternating method was proposed to optimise the difficult problem of advanced Angle selection [22]. At the same time, a drive scheme with high torque current ratio is proposed, which adopts adaptive phase delay compensation to adjust the current in the reversing process [23]. In addition, direct instantaneous torque control was improved to suppress torque ripple [24]. All the above methods can improve the reversing torque ripple to some extent, but it is difficult to be applied because of the complexity of the calculation process caused by the introduction of adaptive controller.

To improve the startup performance of DSEM SG, currents distribution with AAC method is researched in this paper. First of all, the power loss distribution is studied through the established DSEM power loss calculation model. On this base, according to obtained the quantitative relationship between

DSEM power loss and field current, the optimal field current can be achieved, and a currents distribution strategy under certain speed and load torque is proposed, and a torque observer is designed to identify the practical DSEM operating condition. To further improve output torque performance, the optimal advanced commutation angle is analysed and defined, and AAC is proposed to be utilised with the proposed currents distribution strategy. Finally, a series of experiments are carried out on a 12/8-pole DSEM system, and the results verify the correctness and feasibility of the proposed strategies.

2 | THE BASIC OPERATING PRINCIPLE OF DSEM

The diagram of DSEM SG system is shown in Figure 1. At the starting stage, the switch S1 is on, and the starting power supply (battery) supplies power to the DSEM through the full-bridge converter. The DSEM drives the aeroengine to start and run as a motor. After the engine reaches the ignition speed, S1 is disconnected and S2 is on. The engine in turn drives the DSEM, which operates as a generator to supply power to the load. Power generation control can be carried out by adjusting the field current and armature current.

Figure 2a shows the cross-sectional view of a 12/8 pole DSEM, the stator and rotor are both with salient structure, which are laminated by silicon steel sheets. No permanent or any winding are mounted the rotor, the stator slots are embedded with centralised field windings and armature windings. The simple structure contributes to its high reliability under harsh working conditions. Figure 2b shows the power circuits for DSEM driving. Three-phase full-bridge inverter is generally applied for armature windings control, and the field winding is driven by asymmetric half-bridge converter, the two converters are powered by a same direct current (DC) power. Figure 2c shows the “120° three step” conduction rule for DSEM. In order to ensure the stable operation of the electric cycle, three commutation instants should be detected in time.

The output torque T_p ($p = a, b$ or c) of each phase contains reluctance torque T_{pr} and excitation component $T_{p\delta}$ as expressed in Equations (1) and (2), where i_p , L_p are phase current and inductance, respectively, L_{pf} is the mutual inductance between three-phase windings and field winding. In a

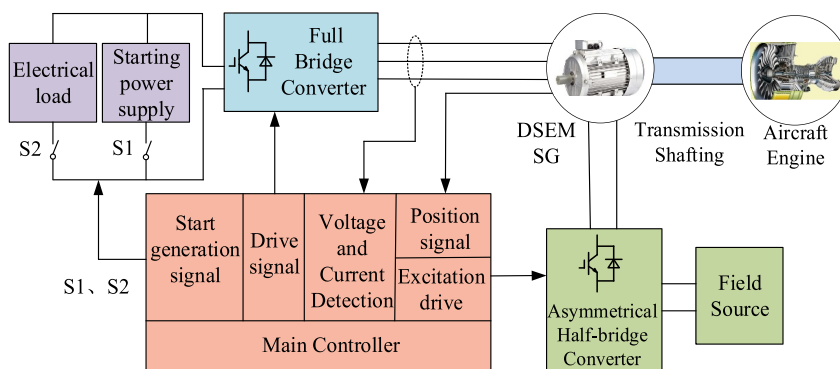
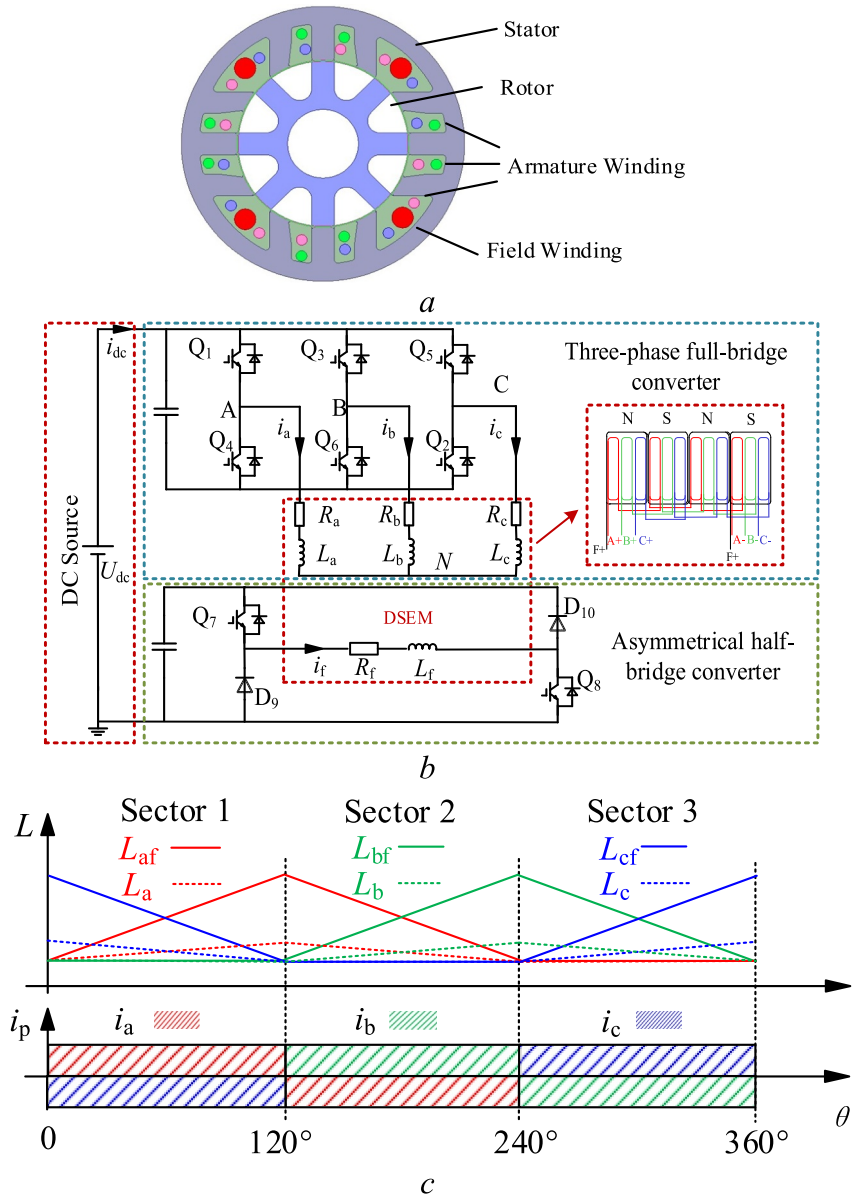


FIGURE 1 Doubly salient electromagnetic machine (DSEM) SG system.

FIGURE 2 Basic operating principle of doubly salient electromagnetic machine (DSEM). (a) Cross section of a 12/8-pole DSEM. (b) Main power circuits of DSEM driving. (c) “120° three step” conduction mode of DSEM.



general DSEM, the turns of field winding are much larger than that of armature winding, so the mutual inductance between the armature winding and the field winding of DSEM is far greater than its three-phase self-inductance, thus the field torque is the major component and the reluctance torque component is ignored.

$$T_{Pr} = \frac{1}{2} i_p^2 \frac{dL_p}{d\theta} \quad (1)$$

$$T_{Pf} = i_f i_p \frac{dL_{Pf}}{d\theta} \quad (2)$$

Figure 3 shows the block diagram of the traditional startup control. Field current is set to the rated value regardless of speed or load conditions. However, since the turns of field winding is much larger than that of armature winding, the field

winding brings lots of power loss especially under light load conditions. Meanwhile, the phase current is controlled as semi-square waveform with SAC, bringing in large power loss as well non-negligible torque ripple. The aforementioned traditional control methods limit the further improvement of DSEM. Therefore, the currents distribution with AAC optimisation strategy based on the minimum loss of DSEM is proposed.

3 | CURRENTS DISTRIBUTION CONTROL FOR DSEM

3.1 | Power loss analysis of DSEM

Due to the limitation of motor structure and materials, it is inevitable to generate losses during its operation. Reducing power loss is the direct way to improve the operation efficiency.

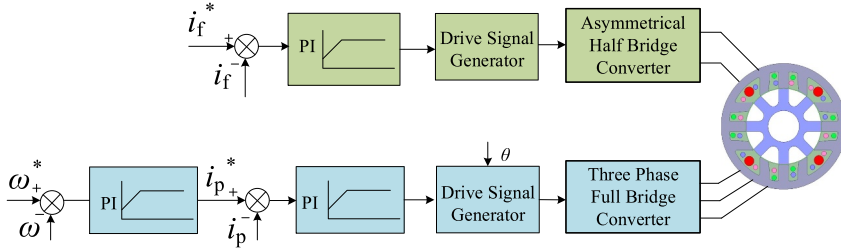


FIGURE 3 The traditional startup control strategy of doubly salient electromagnetic machine (DSEM).

Figure 4 shows the loss distribution diagram of the DSEM, in which P_p and P_F are the energy input from the main power converter and the field power converter, P_{conP} and P_{conF} refer to the loss of the main power converter and the power converter of the field circuit respectively. P_z and P_m are stray loss and mechanical loss of motor. For the entire DSEM system, the above losses account for a relatively small proportion, while iron loss P_{Fe} and copper loss P_{Cu} are the main losses, which endanger the efficiency and service life of the system.

The copper loss of DSEM can be divided into two parts: armature winding copper loss P_{Cup} and field winding copper loss P_{Cuf} which can be expressed as Equation (3). Since the three phases of DSEM are symmetrical, the copper loss can be simplified as Equation (4).

$$P_{\text{Cu}} = P_{\text{Cup}} + P_{\text{Cuf}} = i_a^2 R_a + i_b^2 R_b + i_c^2 R_c + i_f^2 R_f \quad (3)$$

$$P_{\text{Cu}} = 2i_p^2 R_p + i_f^2 R_f \quad (4)$$

where R_p is the resistance of the armature winding.

The traditional calculation of iron loss includes hysteresis loss, eddy current loss, and additional loss. On this basis, the additional loss is considered as a part of eddy current loss, and a binomial calculation model is established.

$$P_{\text{Fe}} = P_h + P_c = k_b B_m^\kappa f + k_c (B_m f)^2 \quad (5)$$

where k_b and k_c are hysteresis loss coefficient and eddy current loss coefficient respectively, and $\kappa = 2$.

In the finite element loss model, the loss when different field currents are used to participate in system control under 500rpm and 3Nm is calculated, and the results are shown in Figure 5. In traditional startup control, it is not optimal to control the field current to the rated value of 6A. Therefore, the purpose of reducing the system loss can be achieved by adjusting the field current. In addition, the acquisition of optimal current needs to fit and calculate the motor loss under corresponding working conditions.

3.2 | Loss coefficient fitting and currents distribution strategy

Due to the complexity of the iron core structure and magnetic field distribution of the motor, the hysteresis loss coefficient

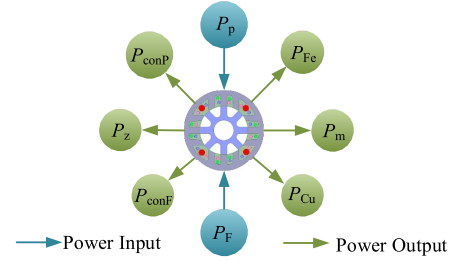


FIGURE 4 The power loss distribution diagram of doubly salient electromagnetic machine (DSEM).

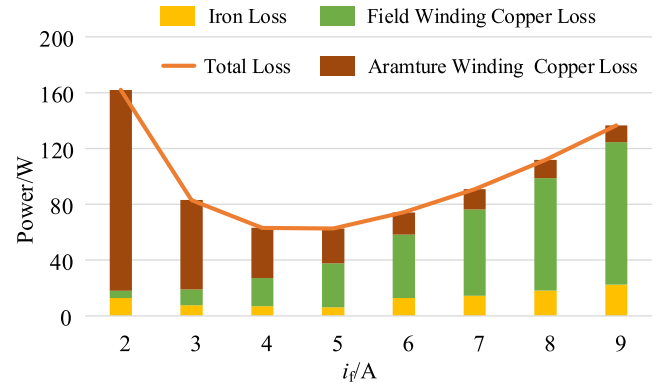


FIGURE 5 Comparison diagram of motor losses under different field current control.

k_b , eddy current loss coefficient k_c and motor magnetic density B_m are difficult to obtain online, resulting in that the iron loss of the motor cannot be directly obtained by simply using the traditional iron loss model. Therefore, the following simplified analysis is carried out.

$$B_m = \frac{B_{\text{max}} - B_{\text{min}}}{2} = \frac{k_\varphi (\varphi_{\text{max}} - \varphi_{\text{min}})}{2} = \frac{k_\varphi i_f (L_{\text{pf max}} - L_{\text{pf min}})}{2} \quad (6)$$

$$f = \frac{\omega}{2\pi} \quad (7)$$

Therefore, the sum of iron loss and copper loss of DSEM can be expressed as Equations (8) and (9).

$$P_{\text{Fe}} = k_{L1}\omega i_f^2 + k_{L2}\omega^2 i_f^2 \quad (8)$$

$$P_{\text{Loss}} = 2i_p^2 R_p + i_f^2 R_f + k_{L1}\omega i_f^2 + k_{L2}\omega^2 i_f^2 \quad (9)$$

where k_φ is the coefficient between magnetic density and magnetic chain, and the iron loss calculation coefficients are

$$k_{L1} = k_\varphi \cdot \frac{(L_{\text{pf max}} - L_{\text{pf min}})^2}{4 \cdot 2\pi} \quad \text{and} \quad k_{L2} = k_c \cdot \frac{k_\psi (L_{\text{pf max}} - L_{\text{pf min}})^2}{4 \cdot 4\pi^2}$$

In order to avoid complex iron loss calculation, loss calculation coefficients k_{L1} and k_{L2} are obtained by least square method. The model parameters are shown in Table 1, and the specific calculation process is as follows.

- (i) Different speed, field current and armature current are input in the ANSYS model to obtain the motor loss and torque information under the corresponding combination.
- (ii) The autoregressive least square method is used for non-linear fitting of the obtained data, and the expression of the objective function ε is established as Equation (10).

$$\varepsilon = \sum (F(\mathbf{k}, \mathbf{x}) - y)^2 \quad (10)$$

where $F(\mathbf{k}, \mathbf{x}) = 2\hat{i}_p^2 R_p + \hat{i}_f^2 R_f + k_{L1}\hat{\omega}\hat{i}_f^2 + k_{L2}\hat{\omega}^2\hat{i}_f^2$, $\mathbf{x} = [\hat{i}_p, \hat{i}_f, \hat{\omega}]$, $y = \hat{P}_{\text{Loss}}$, $\mathbf{k} = [k_{L1}, k_{L2}]$. $[\hat{i}_p, \hat{i}_f, \hat{\omega}, \hat{P}_{\text{Loss}}]$ are respectively the armature current, field current, speed and loss under corresponding working conditions selected in ANSYS simulation.

- (iii) The loss coefficients k_{L1} and k_{L2} are obtained by fitting calculation. Because the calculated data fully considers the influence of operating conditions on the coefficient. Therefore, on the premise of ignoring the change of motor resistance parameters, the values of k_{L1} and k_{L2} do not change with the operating parameters during the actual operation of the motor.

TABLE 1 Parameters of doubly salient electromagnetic machine (DSEM).

Motor parameters	Value
Stator poles/Rotor poles	12/8
Rated DC bus voltage	100 V
Rated power	1 kW
Normal speed	1000 r/min
Minimal/maximal L_p	0.5/3.5 mH
Minimal/maximal L_{pf}	1.6/18 mH
Stator resistance	0.5 Ω
Field winding resistance	1.26 Ω
Field winding inductance L_f	63 mH

The loss calculation coefficient is brought into Equation (9) to obtain the comparison diagram of corresponding actual loss and fitting loss under 1000rpm working condition as shown in Figure 6. The figure shows that the calculation result has a good fitting effect.

When three-phase three state control is adopted, the torque of DSEM can be expressed as Equation (11).

$$T_e = 2T_p = 2i_f i_p \frac{\partial L_{\text{pf}}}{\partial \theta} = C_t i_f i_p \quad (11)$$

In which C_t is the torque coefficient.

Combined with Equations (9) and (11), the field current corresponding to the minimum loss can be obtained.

$$i_f^* = \sqrt[4]{\frac{2T_e^2 R_p}{C_t^2 (k_{L1}\omega + k_{L2}\omega^2 + R_f)}} \quad (12)$$

Therefore, the field current satisfying the minimum loss under the determined working condition can be obtained by using the direct calculation method, so as to realise the currents distribution of the system and apply it to the actual DSEM control system.

3.3 | Torque observer design based on BP neural network

To realise currents distribution, it is necessary to accurately identify the operating condition information for motor control. For the speed information can be calculated by the motor position decoder, but the torque information is limited by the poor observation accuracy of the traditional torque observer, and usually ignores the motor saturation effect. This paper fully considers the non-linear characteristics of the system when the magnetic circuit is saturated, and designs a novel

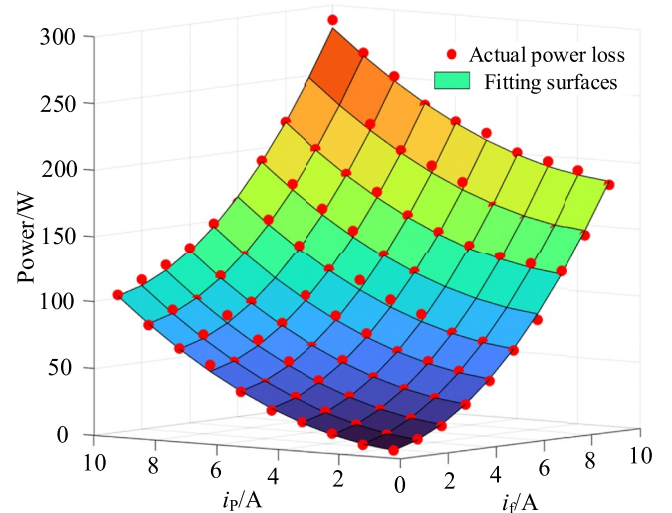


FIGURE 6 Comparison chart of actual loss and fitting loss surfaces.

torque observer. Its algorithm is easy to implement, and its calculation accuracy is high, which can meet the actual control needs.

When considering motor saturation and advance commutation control, C_t can be considered as the coefficient related to field current, armature current and advance angle α . Due to the complex coupling relationship between torque coefficient C_t with i_f , i_p and α , it is difficult to perform linear fitting calculation. Considering the advantages of neural network algorithm in complex non-linear data processing, this paper designs a torque observer to identify torque coefficient based on BP neural network algorithm, fully considering the influence of three-phase three state advance angle conversion on torque coefficient. A three- input single-hidden layer BP neural network is designed as shown in Figure 7. Regarding the selection of the number of hidden layer nodes, this article uses a combination of golden section method and traversal algorithm for calculation. According to the calculation formula shown in Equation (13), different numbers of nodes were traversed, and the calculation results showed that when four nodes were used, the calculation error was the smallest and the effect was the best.

$$N_b = \sqrt{N_{in} + N_{out}} + \alpha \quad (13)$$

where N_b is the number of hidden layer nodes, N_{in} is the number of input layer nodes, N_{out} is the number of output layer nodes, and α is a constant between 1 and 10.

This article uses offline training to train the model based on the obtained data. Divide the 240 sets of data obtained offline, randomly select 180 sets as training data, and the remaining 60 sets as test data. The BP neural network model is trained according to the flow chart shown in Figure 8.

The hyperbolic tangent sigmoid function Tansig is selected as the excitation function, which is defined as $g(x)$ as follows:

$$g(x) = \frac{2}{1 + e^{-2x}} - 1 \quad (14)$$

The root mean square error $RMSE$ function is constructed as the training objective error function.

$$RMSE(y_i) = \frac{1}{m} \sum_{i=1}^m (y_i - y_r)^2 \quad (15)$$

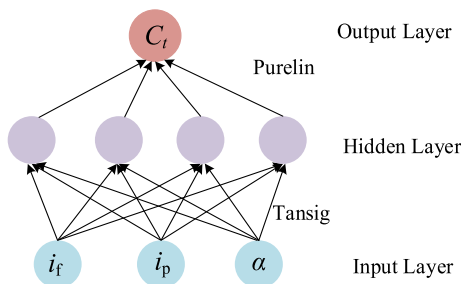


FIGURE 7 Torque coefficient observation model based on back propagation (BP) neural network.

where: y_i is the expected value of the ideal field current given of the BP neural network topology, y_r is the given value of the actual output field current, m is the number of samples.

After offline training, the effect of fitting is shown in Figure 9. The results show that the relative error of the fitting results is within $\pm 3\%$ and the model has good prediction effect. Applying the offline trained model to the online observation, the motor torque information can be obtained in real time.

As shown in Figure 10, the loss calculation coefficient and torque information obtained by offline fitting are brought

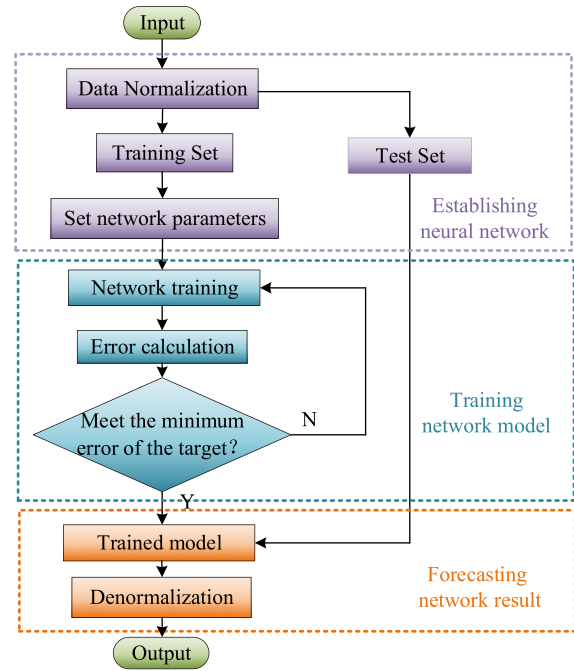


FIGURE 8 Flow chart of establishing and training back propagation (BP) neural network.

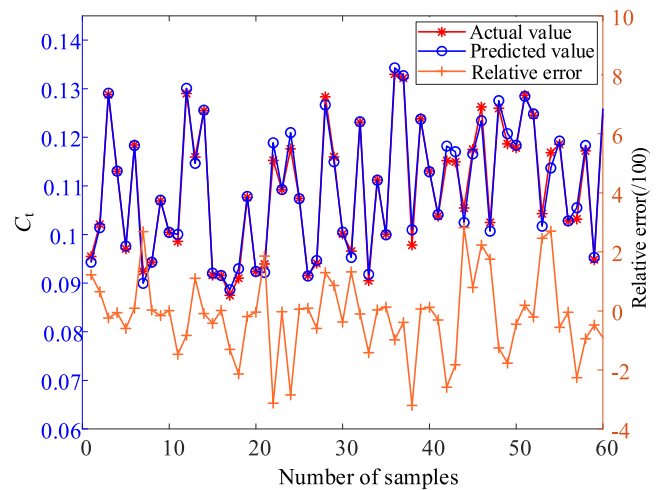


FIGURE 9 Torque coefficient observation model based on back propagation (BP) neural network.

into (12), and the field current setting value i_f^* under corresponding working conditions can be solved online.

The currents distribution strategy is simulated at 1000 rpm and 3 Nm. The data in Table 2 shows that the total loss of the system is significantly reduced after currents distribution. In order to ensure the accuracy and reliability of the data, So in this paper, the average iron loss value in one cycle after the motor stabilisation is selected as a reference value.

4 | ADVANCED ANGLE COMMUTATION CONTROL STRATEGY OF DSEM

4.1 | Analysis of SAC process

As shown in Figure 11, the commutation process includes two processes. Taking 120° commutation point as an example. θ_1 is the angle corresponding to phase A freewheeling, and θ_2 is the angle corresponding phase A current raising to the given value.

(i) During $120^\circ \sim (120 + \theta_1)^\circ$, the currents of A and C phases drop to 0. (ii) During $(120 + \theta_1)^\circ \sim (120 + \theta_1 + \theta_2)^\circ$, the currents of B and A phases rise to the given value i_p^* .

As shown in Figure 12, the equivalent circuit of the commutation process is established, and the mathematical expression is as follows.

$$-U_{dc} - e_a - i_a R - L_a \frac{di_a}{dt} + L_c \frac{di_c}{dt} + i_c R + e_c = 0 \quad (16)$$

where $i_a + i_c = 0$, $i_a > 0$. Ignoring the influence of magnetoresistance back EMF and assuming that the field current is

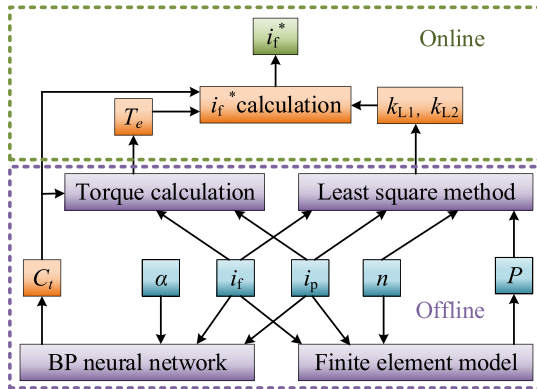


FIGURE 10 Schematic diagram of field current solution.

TABLE 2 Finite element simulation results.

Control strategy	Traditional method	Currents distribution method
i_f/A	6	4.3
i_p/A	4.47	5.78
Copper Loss/W	65.34	56.69
Iron Loss/W	18.11	11.98
Total Loss/W	83.45	68.67

constant, so $e_a = k_{ef}\omega$, Where k_{ef} is the back EMF coefficient and its value is $dL_{pf}/d\theta$. The value of armature winding voltage drop $i_p \cdot R$ is far less than the amplitude of DC bus voltage and back EMF, so its influence can be ignored. Therefore, the freewheeling time and angle are obtained.

$$t_1 = \frac{L_{pmax} + L_{pmin}}{2R} \ln \frac{U_{dc} + 2k_{ef} \cdot \omega + 2R \cdot i_p^*}{U_{dc} + 2k_{ef} \cdot \omega} \quad (17)$$

$$\theta_1 = \omega \cdot \frac{L_{pmax} + L_{pmin}}{2R} \ln \frac{U_{dc} + 2k_{ef} \cdot \omega + 2R \cdot i_p^*}{U_{dc} + 2k_{ef} \cdot \omega} \quad (18)$$

Similarly, the time and angle at which the current rises to a given value can be obtained.

$$t_2 = \frac{L_{pmax} + L_{pmin}}{2R} \ln \frac{U_{dc} + k_{ef} \cdot \omega}{U_{dc} + k_{ef} \cdot \omega - 2R \cdot i_p^*} \quad (19)$$

$$\theta_2 = \omega \cdot \frac{L_{pmax} + L_{pmin}}{2R} \ln \frac{U_{dc} + k_{ef} \cdot \omega}{U_{dc} + k_{ef} \cdot \omega - 2R \cdot i_p^*} \quad (20)$$

In order to simplify the analysis, the change rate of current in the above two processes is approximately considered as k_{p1} , k_{p2} , and the partial derivative of mutual inductance and angle is k_{pf} . On this basis, the torque value can be obtained and shown with 1/3 cycle as an example.

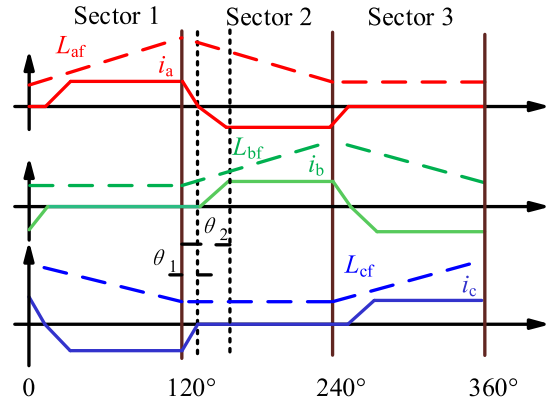


FIGURE 11 Current diagram of doubly salient electromagnetic machine (DSEM) standard angle commutation (SAC).

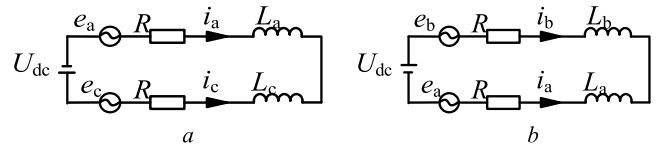


FIGURE 12 Equivalent circuit diagram of standard angle commutation (SAC) process. (a) $120^\circ \sim (120 + \theta_1)^\circ$. (b) $(120 + \theta_1)^\circ \sim (120 + \theta_1 + \theta_2)^\circ$.

$$T_e = \begin{cases} 2k_{pf}i_f i_p^* & \theta_2 \sim 120^\circ \\ -2k_{pf}i_f(i_p^* - k_{p1}\theta_1) & 120^\circ \sim 120^\circ + \theta_1 \\ 2k_{pf}i_f k_{p2}(\theta_2 - \theta_1) & 120^\circ + \theta_1 \sim 120^\circ + \theta_2 \end{cases} \quad (21)$$

During $120^\circ \sim (120 + \theta_1)^\circ$, negative electromagnetic torque is generated, and during $(120 + \theta_1)^\circ \sim (120 + \theta_2)^\circ$, the torque has obvious drop.

4.2 | Analysis of AAC of DSEM and the optimal angle selection

The back EMF will increase with the rise of motor speed. At the same time, the change rate of armature current rise during commutation is low, and the commutation time is long, so a large current gap will be generated, which will cause torque drop and limit the output of the motor. In order to solve this problem, AAC is adopted to increase the output and improve the torque-current ratio of the system.

On the basis of the above analysis, the following three schemes are divided according to the angle of commutation advance. α is the commutation advance angle, β is the angle between A-phase current zero crossing and standard commutation, γ is the angle between A-phase current rising to the given value and standard commutation.

According to Figure 13, the motor torque corresponding to the commutation region under the three schemes can be obtained.

(i) $\alpha < \theta_1$

$$T_e = \begin{cases} 2k_{pf}i_f[i_p^* - k_{p1}(\theta + \alpha - 120^\circ)] & 120^\circ - \alpha \sim 120^\circ \\ -k_{pf}i_f[i_p^* - k_{p1}(\theta + \alpha - 120^\circ)] & 120^\circ \sim 120^\circ + \beta \\ 2k_{pf}i_f k_{p2}(\theta - \beta - 120^\circ) & 120^\circ + \beta \sim 120^\circ + \gamma \end{cases} \quad (22)$$

(ii) $\alpha = \theta_1$

$$T_e = \begin{cases} 2k_{pf}i_f[i_p^* - k_{p1}(\theta + \alpha - 120^\circ)] & 120^\circ - \alpha \sim 120^\circ \\ 2k_{pf}i_f k_{p2}(\theta - 120^\circ) & 120^\circ \sim 120^\circ + \gamma \end{cases} \quad (23)$$

(iii) $\alpha > \theta_1$

$$T_e = \begin{cases} 2k_{pf}i_f[i_p^* - k_{p1}(\theta + \alpha - 120^\circ)] & 120^\circ - \alpha \sim 120^\circ - \beta \\ -k_{pf}i_f k_{p2}(\theta + \beta - 120^\circ) & 120^\circ - \beta \sim 120^\circ \\ 2k_{pf}i_f k_{p2}(\theta + \beta - 120^\circ) & 120^\circ \sim 120^\circ + \gamma \end{cases} \quad (24)$$

The torque ripple ratio is defined as τ :

$$\tau = \frac{T_{rip}}{T_{avg}} \times 100\% \quad (25)$$

In the above three cases, the maximum torque ripple ratio is:

$$\tau_{max} = \begin{cases} \frac{2\alpha + 3\beta}{2(\alpha + \beta)} & \alpha < \theta_{f1} \\ 1 & \alpha = \theta_{f1} \\ \frac{3\beta + 2\gamma}{2(\beta + \gamma)} & \alpha > \theta_{f1} \end{cases} \quad (26)$$

When $\alpha = \theta_1$, negative electromagnetic torque will not be generated and torque ripple ratio is minimum. Therefore, the optimal commutation angle selected in this paper refers to the angle corresponding to the minimum torque ripple ratio that can be generated by the DSEM in the commutation range. The AAC strategy can suppress the torque ripple and improve the torque current ratio of the system.

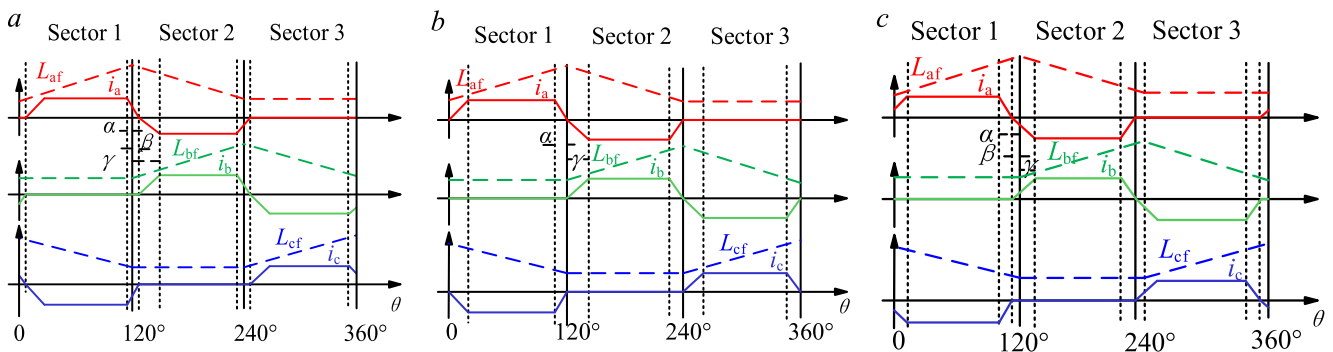


FIGURE 13 Schematic diagram of current and inductance in case of advanced angle commutation (AAC). (a) $\alpha < \theta_1$. (b) $\alpha = \theta_1$. (c) $\alpha > \theta_1$.

4.3 | Optimal control strategy of currents distribution with AAC

As analysed aforementioned, the traditional startup control strategy of DSEM sets the field current as the rated value without considering the change of working conditions, which leads to large losses, and the phase current is controlled as semi-square waveform with SAC mode causes large torque ripple during the commutation process. This paper presents a currents distribution with AAC strategy. The control block diagram is shown in Figure 14. The torque coefficient is calculated by BP neural network algorithm, the currents distribution based on the minimum loss is calculated online and the advanced angle is obtained from a 3-D lookup table based on the minimum commutation torque ripple. A mapping table of different field current, armature current, DC bus voltage, motor speed, and optimal commutation advanced angle is established. The real-time data of the above four physical quantities are obtained by sampling. This method can effectively improve the torque current ratio of the motor, improve the system energy efficiency, and reduce torque ripple.

5 | EXPERIMENTAL VERIFICATION

5.1 | Experimental setup

Figure 15 shows the DSEM SG experimental prototype platform. It mainly contains a 12/8-pole three-phase DSEM, of which the parameters are shown in Table 1, a three-phase full-bridge inverter circuit for DSEM driving, a TMS320F28379D based controller board, sampling and driving circuits, a permanent magnet synchronous motor serving as the load machine which is coaxially connected to DSEM, and it connects to a rectifier bridge and adjustable resistance load, thus the load torque of DSEM can be regulated by the resistance. This

design is closer to the actual motor application environment, with more accurate test value.

And due to the large friction coefficient, the load torque caused by friction cannot be ignored.

5.2 | Experimental results

In the experiment of this paper, the bus voltage is set as the rated value, so the efficiency of the system can be evaluated by DC bus current. In order to avoid the influence of bus current fluctuation on the experimental results, the average bus current of each electrical angle period is applied. In the following experimental tests, each method can operate stably under different working conditions. Therefore, the efficiency performance of the proposed optimal control strategy can be compared by observing and comparing the average bus current corresponding to the three control strategies under different working conditions. At the same time, the torque output per-

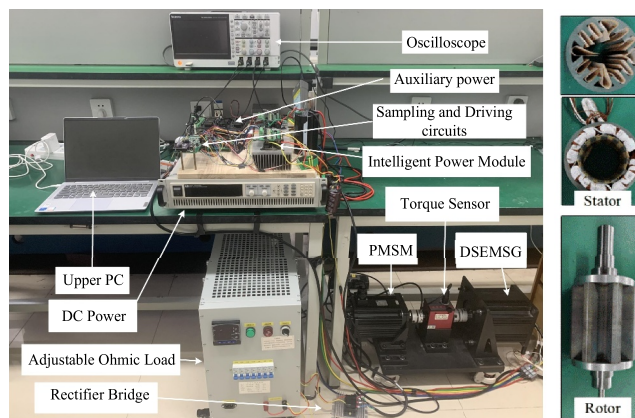
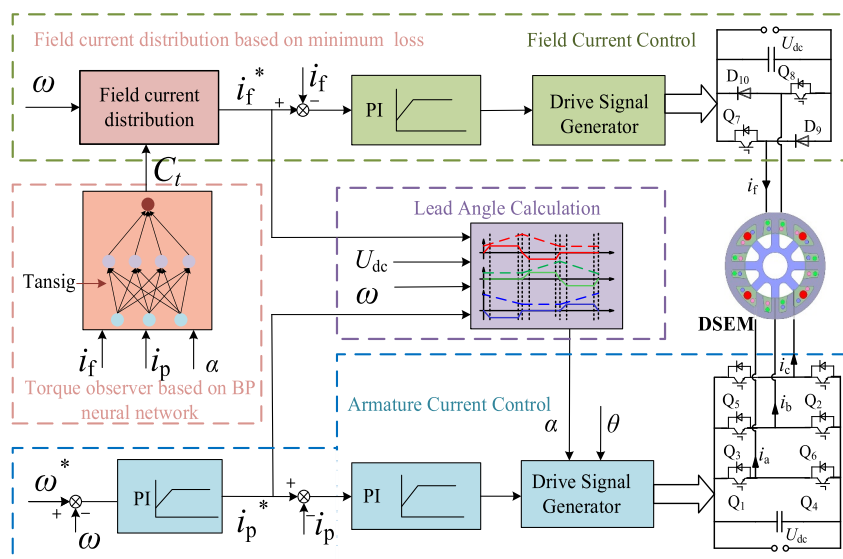


FIGURE 15 The experimental prototype.

FIGURE 14 Optimal control strategy block diagram of currents distribution with advanced angle commutation (AAC) of doubly salient electromagnetic machine (DSEM).



formance of the proposed strategy is characterised by calculating the corresponding torque ripple ratio.

Firstly, the efficiency optimisation performance of the proposed control strategy is tested. As shown in Figure 16, the experiment obtains the DC bus current of the traditional method, currents distribution method and currents distribution with AAC under the same working condition. The field current under the traditional method is rated 6A, and the DC bus current is about 1.2 A. By applying the currents distribution strategy, the field current value corresponding to the minimum loss is involved in the system control, which significantly reduces the loss. On this basis, the currents distribution with AAC is adopted, and the DC bus current value is reduced to 0.6 A, the system efficiency is improved in a certain degree. Although the field current fluctuates, the actual armature

current of the motor will automatically compensate for the fluctuation, so that the output torque and speed characteristics of the motor remain relatively stable.

As shown in Figure 17, the experimental results under load conditions are more obvious. This is mainly reflected in that the given value of the optimal field current calculated by the currents distribution method is relatively improved under large loads and is closer to the rated value numerically. In this case, the optimisation performance of system energy efficiency is more prominent by AAC.

In order to further illustrate the effectiveness of the optimisation strategy under wide speed and load conditions, the following statistical results are measured by the experiment. Figure 18a shows the DC bus current values corresponding to three methods at different speeds with $R_{load} = 48.4 \Omega$ and

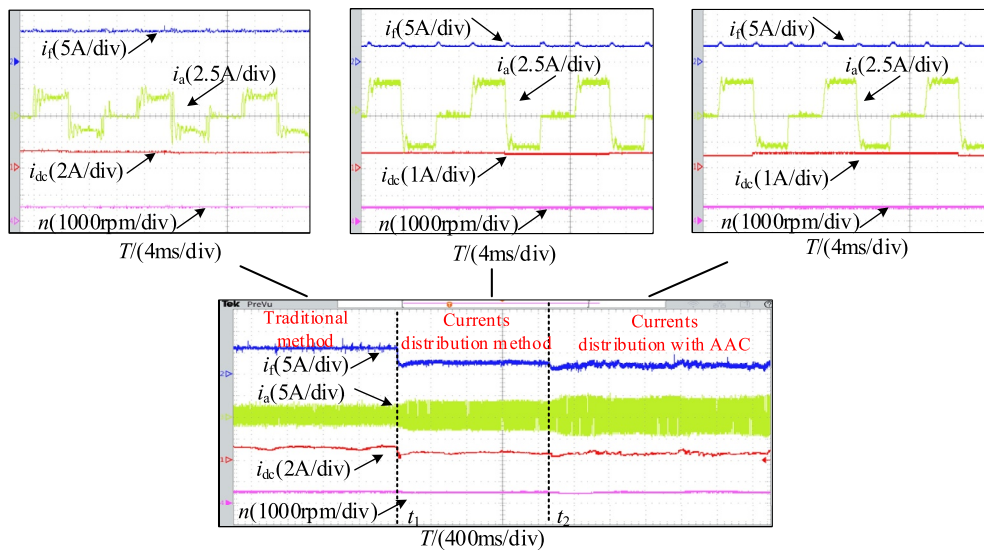


FIGURE 16 Experimental waveforms of direct current (DC) bus current switched by three methods of $n = 500\text{rpm}$ without resistance load.

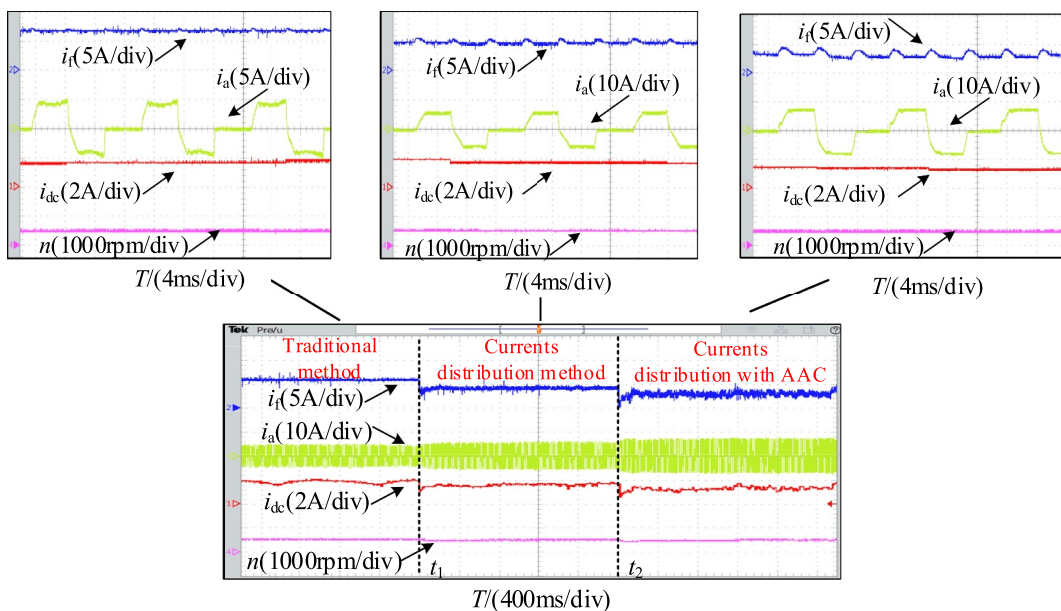


FIGURE 17 Experimental waveforms of direct current (DC) bus current switched by three methods of $n = 500\text{rpm}$ with $R_{load} = 48.4 \Omega$.

Figure 18b shows the DC bus current values corresponding to the three methods at different loads with $n = 500\text{rpm}$. The experimental results show that the currents distribution with AAC can improve the energy efficiency of the system in a wide range of speed and load. On the one hand, when the load is light, the currents distribution strategy is mainly used to reduce the field current and reduce the loss, on the other hand, when the load is heavy, the optimisation efficiency of torque current ratio is mainly improved by AAC.

Then, in order to verify the influence of the optimisation strategy proposed in this paper on the output performance of the motor torque, the following experiments are conducted. The effect of AAC method on torque ripple suppression is verified at first. τ is the torque ripple ratio defined in Equation (25), which is used to characterise the stability of the motor torque output. Under the working conditions shown in Figure 19, compared with SAC, the τ is reduced from 1.75 to 1.05. It is proved that the proposed strategy is effective to optimise the torque output.

In order to further verify the optimisation effect of currents distribution with AAC on the torque output stability. Figure 20 verifies two working conditions respectively with $R_{\text{load}} = \infty$ and $R_{\text{load}} = 48.4 \Omega$. Taking the Figure 20a as an example, the traditional method produces significant torque ripple during the commutation process and the torque ripple ratio is 2.13. When the currents distribution strategy is adopted, the output performance can be significantly optimised. On this basis, the torque ripple ratio is further reduced by adopting the currents distribution with AAC. The torque output stability of DSEM is greatly optimised.

Finally, the dynamic performances are explored. Figure 21 shows dynamic results of currents distribution with AAC strategy when the speed and load changes. In Figures 20a and 21b, there is a sudden change in the speed command value at t_1 , after a regulating duration, the prototype DSEM re-operate stably from t_2 under the new reference speed condition. In Figure 21c,d, the load resistance varies at t_1 , there is a sudden load torque change for DSEM, it is seen under the proposed

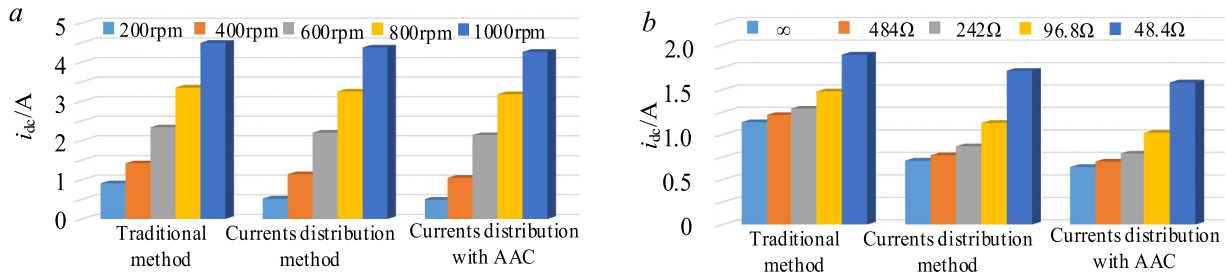


FIGURE 18 The measured direct current (DC) link currents under different speeds and loads. (a) $R_{\text{load}} = 48.4 \Omega$. (b) $n = 500\text{rpm}$.

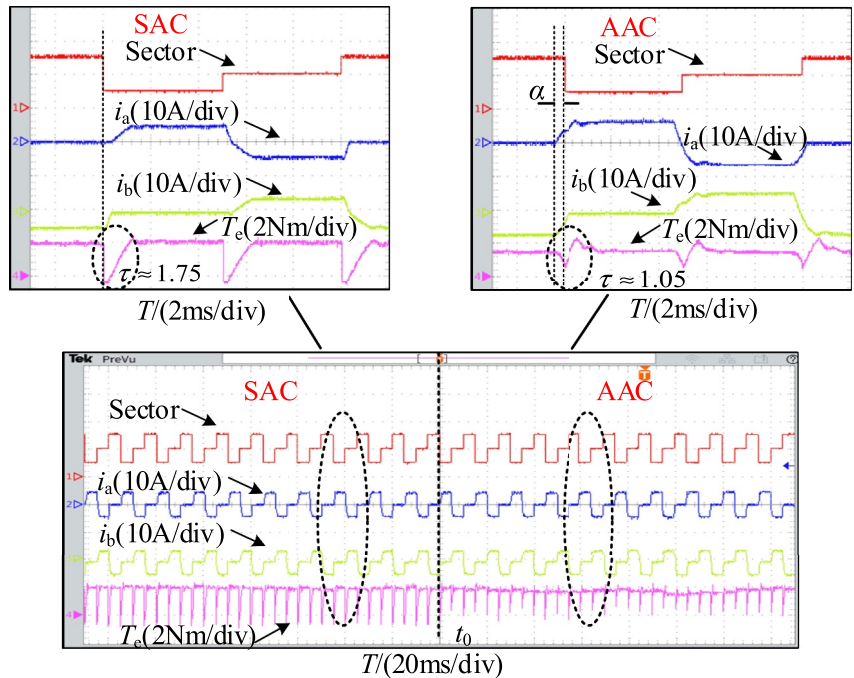


FIGURE 19 Experimental waveforms of torque and phase current with $n = 500\text{rpm}$, $R_{\text{load}} = 96.8 \Omega$.

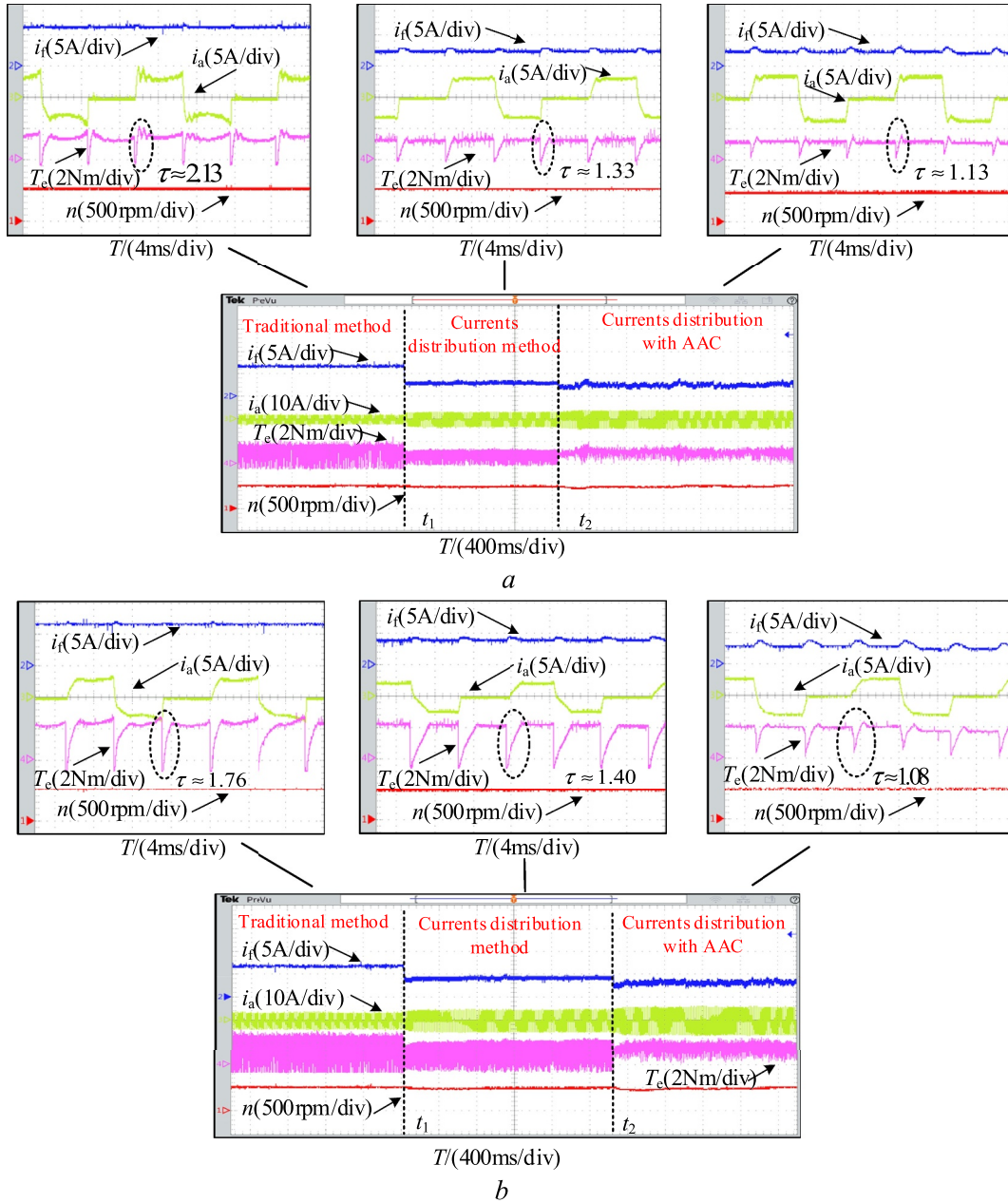


FIGURE 20 Torque waveforms of control strategy switching comparison. (a) $n = 500 \text{ rpm}$, $R_{\text{load}} = \infty$. (b) $n = 500 \text{ rpm}$, $R_{\text{load}} = 48.4 \Omega$.

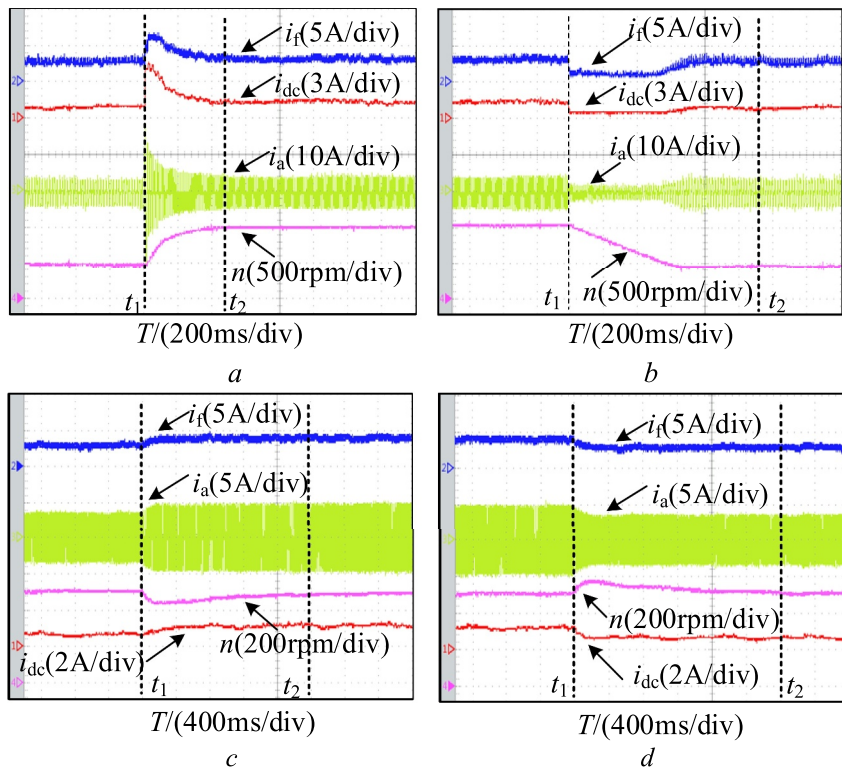
control strategy, satisfactory dynamic performance of load torque changing can be achieved as well.

6 | CONCLUSION

To solve the problems of large power loss and non-negligible torque ripple caused by the conventional DSEM SG startup control method, based on the established finite element power loss calculation model, this paper proposes a currents distribution strategy with advanced angle commutation to improve DSEM SG startup performance. The exhaustive experiments validate the following.

- (i) The currents distribution strategy can reduce the loss of the DSEM SG system over wide ranges of motor speed and load torque conditions, and the application of currents distribution with AAC strategy can further improve system efficiency.
- (ii) In addition to suppressing the cogging torque ripple with distributed currents, the application of currents distribution with AAC can further reduce the commutation torque ripple and improve the output torque amplitude.
- (iii) Under the proposed control strategies, satisfactory DSEM SG startup performance can be achieved under both steady and dynamic processes.

FIGURE 21 The speed and load torque changing dynamic results of the optimised algorithm. (a) $n = 500\text{--}1000\text{rpm}$. (b) $n = 1000\text{--}500\text{rpm}$. (c) $R_{\text{load}} = \infty$ to $R_{\text{load}} = 96.8\ \Omega$. (d) $R_{\text{load}} = 96.8\ \Omega$ to $R_{\text{load}} = \infty$.



AUTHOR CONTRIBUTIONS

Xingwei Zhou: Conceptualisation; Funding acquisition; Resources; Writing-review (lead). **Peixin Liu:** Data curation; Formal analysis; Software; Validation; Writing-original draft. **Shuangxia Niu:** Project administration; Writing-review (equal). **Xing Zhao:** Supervision; Writing-review (equal). **Li Zhang:** Supervision; Writing-review (equal).

ACKNOWLEDGEMENTS

This work was supported in part by the National Natural Science Foundation of China (51907051, 51737006), and in part by Hong Kong Scholar Program (XJ2021015), in part by the open fund Project of Jiangsu Key Laboratory of Power Transmission & Distribution Equipment Technology (2021JSSPd09), and in part by Jiangsu Province Graduate Student Practice Innovation Program (SJCX22_0181).


CONFLICT OF INTEREST STATEMENT

All authors disclosed no relevant relationships.

DATA AVAILABILITY STATEMENT

The data that support the findings of this study are available from the corresponding author upon reasonable request.

ORCID

Xingwei Zhou  <https://orcid.org/0000-0001-5578-0954>
Peixin Liu  <https://orcid.org/0000-0002-5709-5368>

REFERENCES

- Sayed, E., et al.: Review of electric machines in more-/hybrid-/turbo-electric aircraft. *IEEE Trans. Transp. Electrification*. 7(4), 2976–3005 (2021). <https://doi.org/10.1109/tte.2021.3089605>
- Fang, S., Wang, Y., Liu, H.: Design study of an aerospace motor for more electric aircraft. *IET Electr. Power Appl.* 14(14), 2881–2890 (2020). <https://doi.org/10.1049/iet-epa.2020.0507>
- Zhu, L., et al.: Design of power hardware-in-the-loop simulations for integrated starter-generator systems. *IEEE Trans. Transp. Electrification*. 5(1), 80–92 (2019). <https://doi.org/10.1109/tte.2018.2881052>
- Jiao, N., et al.: Field current estimation for wound-rotor synchronous starter-generator with asynchronous brushless exciters. *IEEE Trans. Energy Convers.* 32(4), 1554–1561 (2017). <https://doi.org/10.1109/tec.2017.2698599>
- Shi, L., Zhou, B.: Analysis of a new five-phase fault-tolerant doubly salient brushless DC generator. *IET Electr. Power Appl.* 10(7), 633–670 (2016)
- Wang, K., et al.: A current self-injection based position sensorless control for DSEG with controlled rectification. *IEEE Trans. Ind. Electron.* 37(3), 3308–3320 (2022). <https://doi.org/10.1109/tpel.2021.3113992>
- Liu, W., et al.: Position sensorless control for doubly salient electromagnetic motor based on the terminal voltage. *IET Electr. Power Appl.* 13(12), 2070–2078 (2019). <https://doi.org/10.1049/iet-epa.2019.0227>
- Zhou, X., Zhou, B., Wang, K.: Initial rotor alignment method for doubly salient electromagnetic machine position sensorless startup. *Electron. Lett.* 56(11), 542–544 (2019). <https://doi.org/10.1049/el.2019.3472>
- Chen, Q., et al.: Analysis of multi-phase and multi-layer fractional-slot concentrated-winding on PM eddy current loss considering axial segmentation and load operation. *IEEE Trans. Magn.* 54(11), 1–6 (2018). <https://doi.org/10.1109/tmag.2018.2841874>
- Wang, Q., Niu, S., Luo, X.: A novel hybrid dual-PM machine excited by AC with DC bias for electric vehicle propulsion. *IEEE Trans. Ind. Electron.* 64(9), 6908–6919 (2017). <https://doi.org/10.1109/tie.2017.2682778>

11. Cai, S., et al.: Investigation of novel doubly salient hybrid excited machine with non-overlapped field winding. *IEEE Trans. Energy Convers.* 36(3), 2261–2275 (2021). <https://doi.org/10.1109/tec.2020.3048442>
12. Chen, X., et al.: Model predictive current control of doubly salient electromagnetic machine for current ripple suppression. *IEEE Int. Symp. Predict. Control Electr. Drives Power Electron.*, 1–5 (2019)
13. Yu, L., et al.: Dual-pulse mode control of a high-speed doubly salient electromagnetic machine for loss reduction and speed range extension. *IEEE Trans. Ind. Electron.* 67(6), 4391–4401 (2020). <https://doi.org/10.1109/tie.2019.2931253>
14. Dai, W., et al.: Voltage regulation system of doubly salient electromagnetic generator based on indirect adaptive fuzzy control. *IEEE Access* 5, 14187–14194 (2017). <https://doi.org/10.1109/access.2017.2719048>
15. Wang, A., et al.: Study on optimal current allocation strategy for doubly salient electromagnetic machine based on particle swarm optimization. In: *Proc. IEEE Int. Magn. Conf.*, pp. 1–2 (2018)
16. Zhou, X., Zhang, L., Wu, F.: Operating performance enhancing method for doubly salient electromagnetic machine under light load condition. *IEEE Access* 8, 112057–112065 (2020). <https://doi.org/10.1109/access.2020.3001726>
17. Wang, K., et al.: Minimum field current increment control for doubly salient electro-magnetic generator with improved dynamic performance. *IEEE Trans. Ind. Electron.* 69(5), 4566–4575 (2022). <https://doi.org/10.1109/tie.2021.3082070>
18. Zhou, X., et al.: Research on sensorless and advanced angle control strategies for doubly salient electro-magnetic motor. *IET Electr. Power Appl.* 10(5), 375–383 (2016). <https://doi.org/10.1049/iet-epa.2015.0369>
19. Huang, J., et al.: Self-Optimizing control of commutation angle for DSEM based on three-phase nine-state control. In: *Proc. IEEE ICEMS*, pp. 1–6. Thailand (2022)
20. Wang, Y., et al.: Torque density improvement of doubly salient electromagnetic machine with asymmetric current control. *IEEE Trans. Ind. Electron.* 63(12), 7434–7443 (2016). <https://doi.org/10.1109/tie.2016.2594761>
21. Zhou, X., Zhou, B., Yang, L.: Self-optimizing control of advanced commutation angle for doubly salient electromagnetic machine. In: *Proc. 43rd Annu. Conf. IEEE Ind. Electron. Soc.*, pp. 4403–4407. (IECON) (2017)
22. Jia, W., et al.: Self-tuning control of advanced angles for doubly salient motor drive system. *IEEE J. Emerg. Sel. Topics Power Electron.* 8(2), 1236–1247 (2020). <https://doi.org/10.1109/jestpe.2019.2918260>
23. Bian, Z., Zhang, Z., Yu, L.: Synchronous commutation control of doubly salient motor drive with adaptive angle optimization. *IEEE Trans. Ind. Electron.* 35(6), 6070–6081 (2020). <https://doi.org/10.1109/tpel.2019.2949095>
24. Chen, X., et al.: An improved direct instantaneous torque control of doubly salient electromagnetic machine for torque ripple reduction. *IEEE Trans. Ind. Electron.* 68(8), 6481–6492 (2021). <https://doi.org/10.1109/tie.2020.3003596>

How to cite this article: Zhou, X., et al.: Improved startup control of aero doubly salient electromagnetic starter generator based on optimised currents distribution with advanced angle commutation. *IET Electr. Power Appl.* 1–14 (2023). <https://doi.org/10.1049/elp2.12338>